

Measurements of gas temperatures at 100 kHz within the annulus of a rotating detonation engine

Keith D. Rein¹ · Sukesh Roy¹ · Scott T. Sanders² · Andrew W. Caswell³ · Frederick R. Schauer³ · James R. Gord³

Received: 23 March 2016 / Accepted: 13 January 2017 / Published online: 10 March 2017
© Springer-Verlag Berlin Heidelberg 2017

Abstract Cycle-resolved measurements of H₂O temperatures and number densities taken within the detonation channel of a hydrogen—air rotating detonation engine (RDE) at a 100 kHz repetition rate using laser absorption spectroscopy are presented. The laser source used is an MEMS-tunable Vertical-Cavity Surface Emitting laser which scans from 1330 to 1360 nm. Optical access into and out of the RDE is achieved using a dual-core fiber optic. Light is pitched into the RDE through a sapphire window via a single-mode core, retroreflected off the mirror-polished inner radius of the RDE annulus, and collected with the multi-mode fiber core. The resulting absorption spectra are used to determine gas temperatures as a function of time. These measurements allow characterization of the transient-temperature response of the RDE.

1 Introduction

Detonations are an extremely efficient means of combusting a fuel-oxidizer mixture and releasing its chemical-energy content. A detonation is a supersonic combustion wave; as a result, it is a much more energetic process than deflagration and produces large overpressures. The use of detonation combustion is of significant interest as a means

of increasing cycle efficiency and reducing the cost and complexity of propulsion systems [1].

Rotating detonation engines (RDEs) have a disk-like combustion chamber, where reactants are fed from the bottom and are consumed as a detonation wave continuously propagates circumferentially around the annulus. RDEs have several inherent advantages over the more widely studied pulse detonation engines (PDEs). Although PDEs are operable over a wide range of conditions and Mach numbers, they require the repeated use of a robust detonation initiator. In addition, the mechanics involved with purging and refueling the detonation chamber restrict PDEs to operating frequencies on the order of 100 Hz or less. This, in turn, limits the ability of the PDE to scale to higher thrust levels and produces unfavorable vibrational effects. RDEs, on the other hand, require only a single detonation initiation and have cycle frequencies in the kHz range, which greatly reduce the adverse vibrational effects inherent in the PDE concept [2], produce a much more continuous level of thrust, and result in a much higher thrust-to-weight ratio [3].

Several studies have been conducted over the years involving diode-laser absorption-spectroscopy measurements in detonation-based devices. The vast majority of these measurements has been performed in PDEs. For example, a sensor that was based on rapidly swept, vertical-cavity surface-emitting lasers (VCSELs) and cesium-vapor seeding has been used in the past to determine temperature in a PDE following a detonation wave [4]. H₂O absorption-spectroscopy techniques employing both wavelength-division multiplexing [5] or tuning one [6] or multiple [7] time-division-multiplexed diode techniques have also been used in PDEs to characterize the detonation process. In RDEs, however, laser-spectroscopy measurements to date have been limited to measuring the post-detonation exhaust

✉ Keith D. Rein
kdrein@gmail.com

¹ Spectral Energies, LLC, 5100 Springfield St. Suite 301, Dayton, OH 45431, USA

² University of Wisconsin-Madison, 1500 Engineering Dr, Madison, WI 53706, USA

³ Air Force Research Laboratory, WPAFB, Dayton 45433, USA

gases at the combustor exit [8, 9]. The objective of the present study was to make non-intrusive measurements of gas temperatures and H₂O concentrations within the RDE channel, where the detonation occurs for multiple cycles at sufficient bandwidth to temporally resolve the individual cycles. To our knowledge, these in-situ measurements are thought to be the first such measurements of their kind.

2 Experiment design

2.1 Laser source

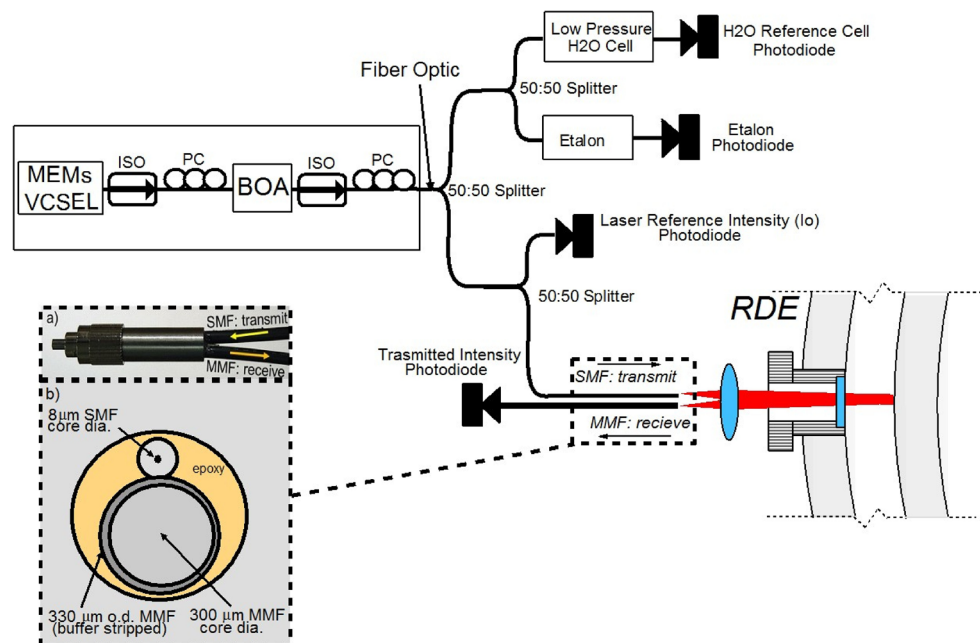
The optical-measurement strategy chosen for this study was laser absorption spectroscopy, covering the $\nu_1 + \nu_3$ rovibrational water band using a single, high-repetition rate, broadly tuning, vertical-cavity surface-emitting laser (VCSEL) tuned by any electrostatically driven micro-electro-mechanical system (MEMS) mirror [10]. MEMS-tunable VCSELs have been available for more than 10 years [11] and have recently demonstrated spectroscopic measurements of H₂O at high-kHz repetition rates [12] and overall scan repetition rates of more than a MHz [13], making them a viable tool for cycle-resolved measurements within an RDE.

Although multiplexed discrete-wavelength [14] or piecewise-continuous swept sources [15] can be optimized to monitor only those wavelengths in the H₂O absorption spectrum that provides the highest temperature sensitivity, the relatively narrow spectral coverage of these sources restricts the range of operating conditions that can be satisfactorily measured, especially in higher pressure gases

in which the collisional broadening of the H₂O absorption features necessitates broader spectral coverage. Multiplexed systems typically are designed to be operated within a relatively narrow range of gas conditions; hence, such sensors were deemed to be unsuitable for the wide range of pressures and temperatures expected within the RDE. The single MEMS VCSEL used for the present measurement, on the other hand, was capable of continuous sweeps of 7325–7520 cm⁻¹ (1335–1365 nm) at repetition rates of 100 kHz, covering thousands of spectral features. As a result, spectral features with temperature sensitivity over the entire range of conditions could be probed using a single compact source. In addition, wavelength-dependent baseline errors caused by effects, such as beam steering within the measured gas, could be assessed and compensated for much more easily with the broad continuous scans. Fourier-domain mode-locking lasers (FDML) have also demonstrated these sweep rates and spectral coverage in high-pressure combustion [16]; however, the FDML linewidths in the GHz range restrict these sources to well above atmospheric pressure, and the inherent multi-mode nature of the source requires careful referencing strategies to overcome modal noise. The MEMS-tunable VCSEL has a much narrower linewidth (<600 MHz [12]), is single-mode, and is less susceptible to spectral drift as compared to the FDML and, thus, was deemed a superior light source.

The schematic of the experimental setup is shown in Fig. 1. The core of the system was a MEMS-VCSEL-swept source (Thorlabs SL1310V1SP4) with a 30-nm (195-cm⁻¹) scan bandwidth centered at 1345 nm (7435 cm⁻¹). The laser-scan repetition rate was set at 100 kHz with a 70% duty cycle, resulting in an average wavelength sweep rate

Fig. 1 Experimental Schematic. An MEMS-tunable VCSEL produces broad wavelength sweeps and is amplified by a booster optical amplifier (BOA). The output is split twice using three 50:50 fiber beamsplitters. One beam is used as the reference beam I_0 (Ref. PD); two beams are used to determine the relative and absolute wavelength position (Etalon PD, Cell PD, respectively). The final output is transmitted to the RDE. There, the SMF (single-mode fiber) of a dual-core fiber optic pitches light into the RDE through a sapphire window in the outer body. The light is retroreflected off the inner body of the RDE and is subsequently collected with the MMF (multi-mode fiber) and recorded (Meas. PD)



of $\sim 23,700 \text{ cm}^{-1} \text{ s}^{-1}$. The output from the MEMS VCSEL was amplified using a booster optical amplifier (BOA) (Thorlabs BOA1036S) to produce $\sim 22 \text{ mW}$ of output. This output was split twice using three 50:50 fiber beam splitters to produce four identical laser outputs. The first of these outputs was coupled directly into a InGaAs photodiode (GPD Optoelectronics GAP544) to provide the reference (I_0) laser signal, whereas two additional outputs were coupled into a 3-mm-thick solid-plane CaF etalon and a 15-Torr H_2O gas cell (Wavelength References) to monitor the relative wavelength axis and absolute wavelength, respectively. The final output was transmitted via single-mode-fiber (SMF) optic cable to the RDE.

2.2 Rotating detonation engine

Measurements were performed at the Detonation Engine Research Facility of the Air Force Research Laboratory using a modular research RDE [17, 18]. A diagram of the RDE is shown in Fig. 2. The RDE is designed around a simple annular detonation channel, with oxidizer and fuel plenums positioned on the side and bottom of the channel, respectively, to promote mixing and produce a homogenous mixture within the detonation channel. These reactants flow axially within the combustion channel, the detonation propagates tangentially around the annulus, and the products are exhausted aft. Fuel is injected from a plenum through 120 holes with diameters of 0.89 mm that are spaced evenly on a circle with a circumference (134-mm diameter) located near the inner edge of the annular detonation channel. The air is injected through a circumferential slot (123-mm diameter) that is located on the inner body. The inner and outer diameters of the annular detonation channel are 138.7 mm (5.46 in) and 153.9 mm (6.06 in),

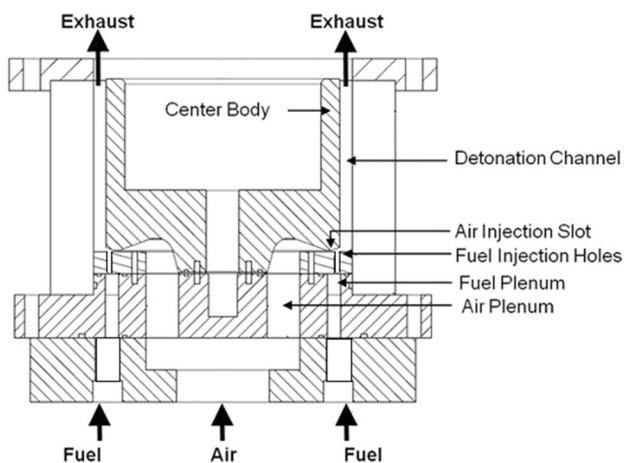


Fig. 2 Diagram of the modular RDE. The air is injected via the outer plenum and fuel is injected via holes in the bottom plenum. The products are exhausted aft

respectively, resulting in a channel width of 7.6 mm (0.30 in). The axial length of the detonation channel is 101.6 mm (4.0 in). Pre-combustion equivalence ratios are controlled by adjusting the mass-flow rates of either the fuel or the oxidizer. Access ports are located in the outer body both circumferentially and axially to facilitate the placement of instrumentation, such as pressure transducers and ion probes into the annulus. Hydrogen and air flow are established and stabilized prior to the initiation of the detonation. The detonation is initiated using a spark-ignition pre-detonator that burns pre-mixed hydrogen and oxygen.

2.3 Optical access

Optical access into the RDE channel was accomplished using in a 1-mm-thick, 6-mm-diameter optical sapphire window that was epoxied into a self-sealing bolt, which was then placed in an instrumentation port located in the outer cylinder of the RDE. The RDE inner-cylinder surface parallel to the sapphire window was mirror polished to a surface reflectivity of $\sim 65\%$ at 1360 nm. An aspheric lens (Thorlabs AL1210-C), translation stage (Thorlabs LM1XY), and FC/APC fiber adapter (Thorlabs SM1FCA) were fixed external to the sapphire window to facilitate optical alignment. All optical pathways, except for the RDE annulus, were purged with nitrogen to eliminate spectral contamination from water vapor in the atmosphere. A custom FC/APC connector containing both a single-mode (SM) and a multi-mode (MM) fiber, described in detail in [7], was used both to transmit and to receive the optical signal. With the use of this setup, light from the MEMS VCSEL was pitched radially into the RDE through the sapphire window (see Fig. 1), retroreflected back along the same optical axis, collected via the MM fiber optic, and measured using a photodiode that was bonded to the fiber to reduce the effects of modal noise [19]. The analog voltage signals from the photodiode amplifiers (Thorlabs PDA10CF) were simultaneously digitized using a 200-MS s^{-1} 16-bit digitizer (*GaGe Razor 16CSE1643*) for transfer to a personal computer for post-processing.

2.4 H_2O -absorption thermometry strategy

Temperature and H_2O -molar-density results were obtained through fitting the experimental data to simulated absorption spectra in a manner similar to that proposed by Kranendonk et al. [20]. First, since the data-acquisition system was located within a control room that was tens of meters away from the RDE, various temporal delays were introduced into the recorded signals, based on the distance between each photodiode amplifier and the data-acquisition system. As a result, the recorded signals had to be time shifted to eliminate these relative delays. An example of the

time-shifted signal from a single laser scan is displayed in the top panel of Fig. 3. Next, it was necessary to identify and correct the voltage offsets caused by thermal emission from the high-temperature gases in the test section or from voltage bias in the photodiodes, preamplifiers, or data-acquisition-system electronics in both the measurement and reference signals. Then, the base-e absorbance was calculated by applying the Beer–Lambert relation to the measured data.

The absorption spectra were converted from a time basis to a relative-wavenumber basis by mapping the etalon data to the absorbance data. The relative-wavenumber axis was then converted to an absolute-wavenumber axis by shifting a peak measured in the low-pressure H₂O reference cell to the corresponding peak location predicted by an HITRAN [21] simulation. The final step in preparing the measured spectra was to correct the wavelength-dependent baseline caused by beamsteering. The baseline trend was determined automatically by means of an algorithm described in Schulze et al.

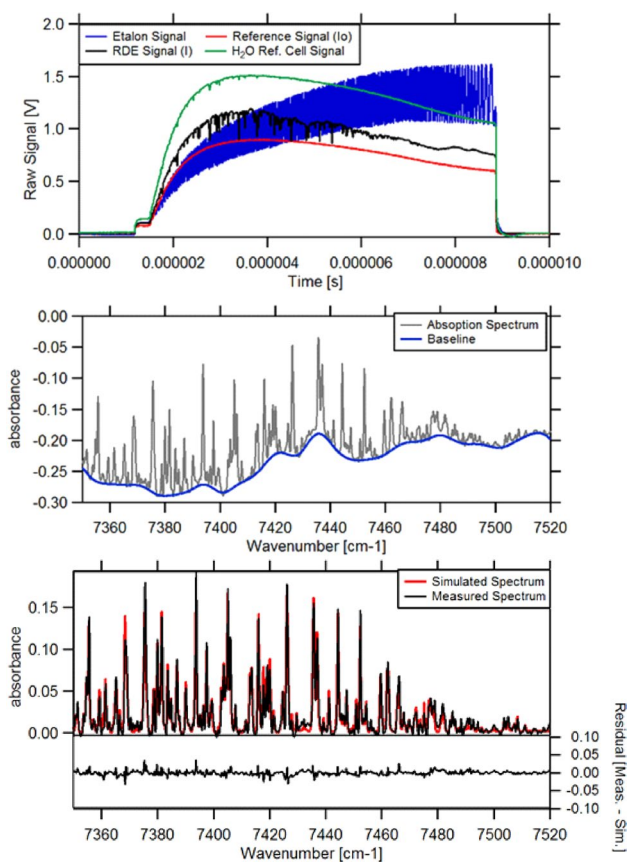


Fig. 3 Top panel measured signals for the laser reference beam, RDE probing beam, and the etalon (for wavelength monitoring) for a single scan of the MEMS—VCSEL. Middle panel corresponding absorption spectrum and the calculated baseline. Bottom panel baseline-fitted absorption spectrum with the best-fit simulated spectrum correspond to a temperature of 1235 K

[22] using a third-order polynomial and then subtracted from the measured absorption spectra. The middle panel of Fig. 3 demonstrates the absorption spectrum calculated from the previously shown raw data and its corresponding baseline fit.

For inferring the gas properties from the processed experimental spectra, a database of simulations assuming a Voigt [23] lineshape profile calculated from the HITEMP [24] line list was compiled that spanned a temperature range of 300–3000 K and Lorentzian half widths 0.1–1 cm⁻¹. Because the digitizer had a –3 dB bandwidth at 125 MHz, the resulting spectral resolution was not sufficient to resolve the H₂O-absorption lineshapes fully without instrumental broadening. To characterize this instrumental broadening, measurements of low-pressure H₂O in the fiber-coupled reference cell were compared to a simulation at the cell conditions (300 K and 15 Torr). Then, when the measured data were processed, each HITEMP simulation was both convolved with the estimated instrumental-broadening function and subjected to the baseline removal procedure that was identical to that employed with the experimentally obtained spectra before an attempt was made to identify the closest matching simulation. This treatment was applied to ensure that the real spectral information deleted from the experimental data would also be removed from the simulated data prior to comparison.

An iterative, least-squares fitting routine was used to determine the best match between each experimentally obtained spectrum and the database of simulated spectra. First, a best-guess Lorentzian half-width was assumed for the simulated spectra, with the guess value being assigned the value of the previous frame result. For the first frame in a data set, the (best) guess was manually set through visual inspection. Using this initial-guess broadening coefficient, a best-fit temperature was found by minimizing the mean-square error (MSE) of a least-squares fit between the measured spectrum and the previously described database subset of simulated spectra over the range of temperatures. The fitting scheme was then repeated using the best-fit temperature from the previous iteration to find a new best-fit broadening coefficient. A final iteration was then performed to find the final best-fit temperature using the best-fit broadening of the previous iteration. The bottom panel in Fig. 3 shows the post-processed measured spectrum, the corresponding best-fit simulated spectrum, and the residual error between measured and simulated spectra.

3 Measurements

3.1 Sensor characterization in a laboratory flame

A Hencken calibration burner was used to produce steady H₂/air diffusion flames for a range of equivalence ratios

to characterize the sensor performance in a similar flame environment as the RDE. The Hencken burner consists of a 50.8 mm × 25.4 mm rectangular array of hypodermic fuel and oxidizer tubes that encourage rapid mixing of fuel and oxidizer components at the exit plane of the burner. The burner array is bordered by a 12.7 mm wide set of nitrogen gas co-flow tubes that help to improve flame stability and isolate the flame from the surrounding room air. Details of the burner can be found in Woolridge et al. [25]. The gas flow rates were regulated using MKS mass-flow controllers, and calibration was performed with a DryCal DC-2 (Bios International Corporation) flowmeter. The air was set at a constant flow rate of 48.8 standard liters per minute for all equivalence ratios, and the hydrogen flow rates were adjusted accordingly to achieve the desired equivalence ratio. The nitrogen flow rate was set, such that the exit velocity of the co-flow matches the combined exit velocity of the reactants.

The MEMS-VCSEL source was operated at 10 kHz repetition rate and was used to determine flame temperatures and H₂O concentrations in the Hencken burner for equivalence ratios ranging from $\phi = 0.5$ –1.3. Multiple beams were used to determine the degree to which the boundary layer interface between the combusting gases and the nitrogen co-flow biased the inferred temperature of the measurement. Two beams were pitched orthogonally across the flame 12.5 mm above the burner surface, so that they each bisected the rectangular flame. The path lengths of the short (I_{short}) and long (I_{long}) beams were 25.4 and 50.8 mm, respectively. During post-processing, two absorption spectra were calculated for each equivalence ratio. Both absorption spectra were calculated using I_{long} as the transmitted intensity; however, the reference beam (I_0) differed. In the first case, the traditional reference beam was used for I_0 , resulting in an effective path length (EPL) of 50.8 mm. The second case, however, replaced I_0 with I_{short} , thereby effectively subtracting the effects of the outer 12.7 mm of each side of the flame from the resulting absorptions spectra and resulted in an EPL of 25.4 mm.

The measured temperatures calculated from both the 25.4 mm and the 50.8 mm EPL absorption spectra are shown in Fig. 4. In addition, the expected equilibrium temperatures for hydrogen/air diffusion flames are also shown. The NASA Computer program CEA (Chemical Equilibrium with Applications) [26] was used to estimate the equilibrium flame temperatures and H₂O concentrations for the conditions studied. For the purpose of the calculations, the reactants were assumed to be at 1.0132 bar and 298.15 K and combustion was set at a constant pressure. Each datapoint represents the best-fit temperature and concentration determined from spectra averaged from 100 sequential laser-scan cycles. Although the above graph shows the measured temperatures for averaged spectra,

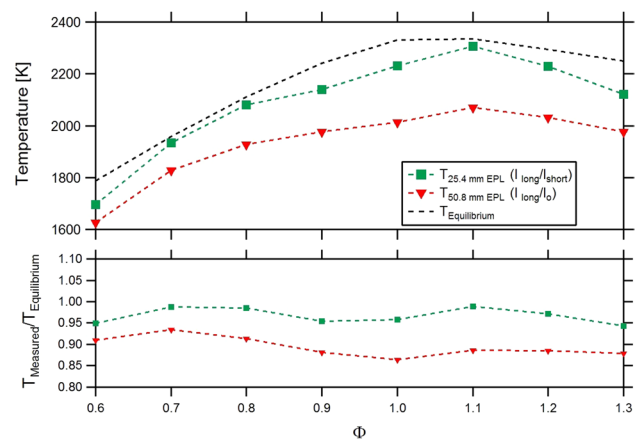


Fig. 4 *Top panel* measured flame temperatures for both the short EPL path (25.4 mm) and long EPL path (50.8 mm) beams. *Bottom panel* measurement temperature bias relative to the adiabatic flame temperature for both the short and long path beams

the cycle-to-cycle variance of inferred temperature from individual scans was very low, especially in the 50.8 mm EPL case. The cycle-to-cycle standard deviation of inferred flame temperatures over those 100 scans was found to be less than 0.25% (± 6 deg. K) at $\phi = 1.0$ for the 50.8 mm EPL case. The cycle-to-cycle variance of the 25.4 EPL case was found to be higher (± 20 deg. K). This is a consequence of both the lower total absorption that results from the shorter EPL as well as the higher noise content in the absorption spectra produced from the addition of path dependent noises, such as beamsteering into the spectra from I_{short} .

As can be seen from figure, utilizing only the center 25.4 mm section of the flame, the measured temperatures collected by the MEMS VCSEL are within approximately 5% of the estimated adiabatic flame temperatures over the entire range of fuel/air equivalence ratios. This consistent temperature deficit relative to equilibrium calculations can most likely be attributed to a combination of radiative losses within the combustion gases, incomplete mixing of the reactants or convective heat losses to the burner surface. By including the outer boundary layers of the flame, the inferred gas temperatures are decreased by an additional 5%, most likely the result of boundary layer interactions between the reacting flows and the nitrogen co-flow.

3.2 Measurement in the RDE

The MEMs VCSEL and accompanying data-acquisition system provided measurements of gas temperature and H₂O number densities at 100 kHz within the detonation channel of the RDE. Hydrogen was used as the fuel, because it is easily detonable, and the oxidizer was air. The data acquisition was triggered off the pre-detonator spark-initiation trigger signal, which preceded the actual

pre-detonator initiation by 3 ms. The RDE was operated for a total time of 0.5 s. The channel width in the RDE was fixed at 0.76 cm; hence, the effective path length for the measurement was 1.52 cm. The height of the air slot was set at 1.78 mm to produce an air-injection area of 6.92 cm². Measurements were performed at axial locations of 25.4 and 50.8 mm aft of the fuel plenum (upstream and downstream axial locations, respectively). Air mass-flow rates ranged from 0.15 to 0.86 kg s⁻¹. These test conditions were chosen to match the conditions of previously obtained chemiluminescence images taken in an RDE of similar design, as outlined in Rankin et al [27]. Background absorption spectra were obtained at several points during the measurement campaign to determine the amount of residual water that was present in the optical paths of the laser system. Based on these background spectra, it was clear that spectral contamination from ambient H₂O vapor was negligible and, thus, that any measured H₂O absorption occurred within the RDE detonation channel. The flowfield was assumed to be uniform along the line-of-sight as the detonation wave propagates tangentially relative to the beam direction.

3.3 Results

An example of the measured temperature and concentrations versus time obtained at the upstream axial location is shown in the left side of Fig. 5. The measured spectra for $t=0.0029$ s (Panel a), 0.00310s (Panel b), 0.00711s (Panel c), and 0.00716s (Panel d) are shown in the four panels on the right side of Fig. 5. As shown in the figure, prior to the ignition of the pre-detonator, ambient-temperature water vapor is indicated in the measured spectra (Panel a). Since the air was dried prior to being injected into the RDE, this measured water vapor is probably the result of the vaporization of residual trapped H₂O in the RDE that was produced during the previous firings. A massive spike in the measured temperature is observed just after 3 ms when the pre-detonator is ignited. For most test conditions, this initial temperature spike produced the highest overall measured temperatures (2110 K for this test condition). After this initial temperature spike, the measured temperature decreases precipitously as fresh cold reactants fill the channel and replace the hot gases at the measurement location. As the detonation wave passes the measurement location a second time, a second spike in temperature is observed. Once again, the temperature decreases as fresh charge replaces the combusted gases, and the process is repeated.

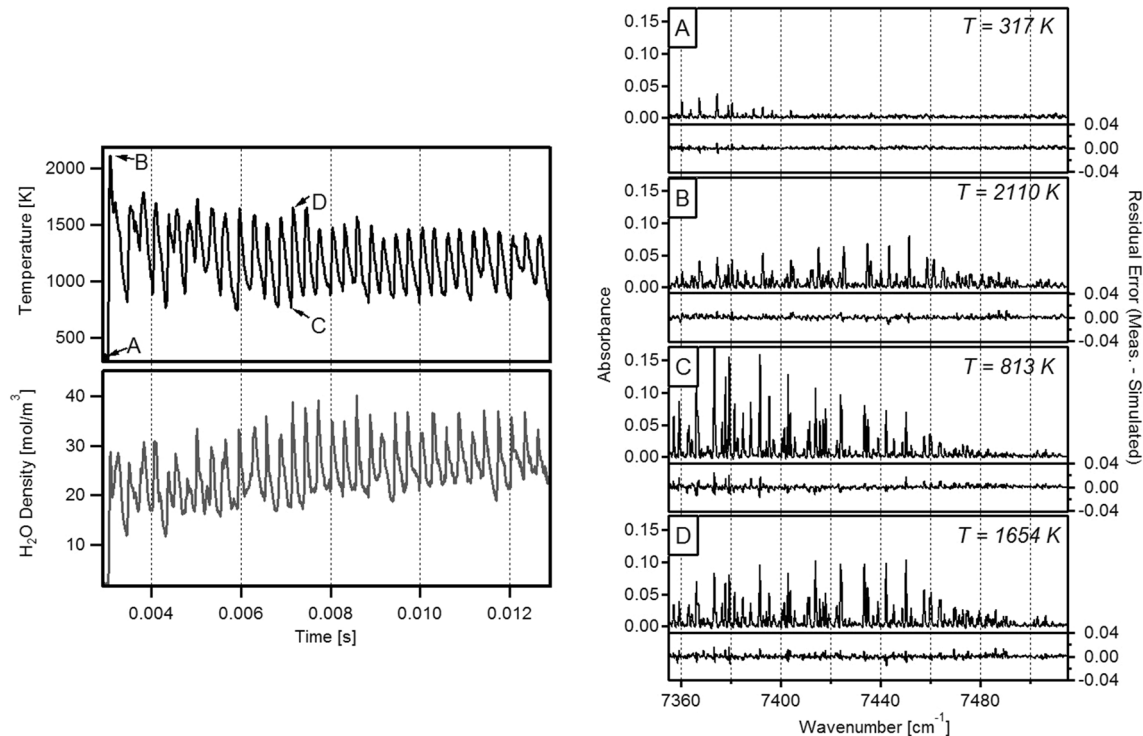


Fig. 5 *Left* measured temperature and H₂O densities in the RDE versus time. *Right* selected measured spectra for $t=0.0029$ s (a), 0.00310s (b), 0.00711s (c), and 0.00716s (d) after pre-detonator trig-

ger initiation. The residual error of the fit (Measured-Simulated) is plotted below each absorption spectrum. The air mass-flow rate for this condition was 0.61 kg s⁻¹ and $\Phi=1.01$

Some variability in wave speed and the range of temperature fluctuations is observed early in the RDE cycle. These fluctuations are probably due to the initial increase in the backpressure within both the air and the fuel plenums produced by the detonation wave [28]. After several initial passes, the plenum pressures equilibrate, and the detonation wave stabilizes within the channel. The result is a cyclical fluctuation in temperature, where a large spike in temperature is observed (Panel d), followed by a steady decline in temperature as fresh charge replaces the combusted gases (Panel c).

3.4 Effects of air mass-flow rate on measured temperature

Figure 6 shows the steady-state temperature and molar-density fluctuations in the RDE detonation channel at the upstream measurement location for four air mass-flow rates (MFR) early in the RDE measurement (8–11 ms after pre-detonator spark trigger). The air-injection slot width (1.78 mm) and equivalence ratio ($1.00 \pm 0.01/-0.03$) are held constant to isolate the effects of the air MFR on the measured temperature at that location.

As shown in Fig. 6, for low MFR conditions (0.15 kg s^{-1}), gas temperatures remain below 600 K and do not show a cyclical sharp rise in measured temperature. The chemiluminescence imaging outlined in [27] indicated that the height of the detonation increased significantly as the air MFR increased from low (0.15 kg s^{-1}) to intermediate (0.32 kg s^{-1}) values. The observed detonation-wave height for this MFR is well below the axial location of the

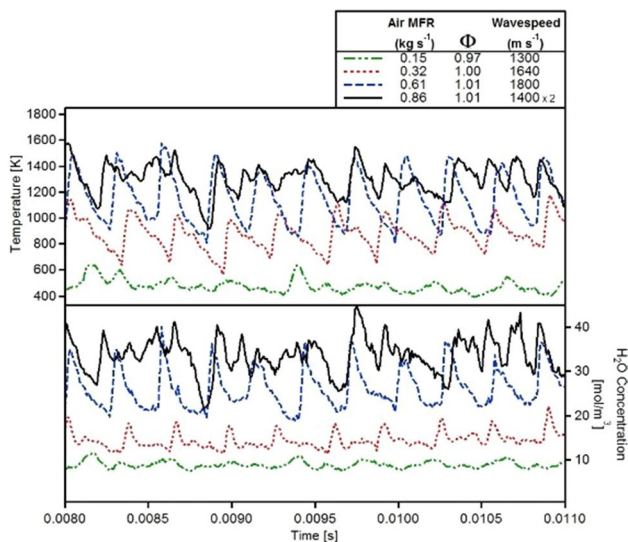


Fig. 6 Measured temperatures and H_2O molar density versus time for four air mass-flow rates. The air-slot thickness and equivalence ratio are held roughly constant

measurement. The measured H_2O spectra for this MFR condition most probably result from the trailing oblique shock containing the combusted products that follows the detonation in the RDE rather than from the actual detonating mixture. Also supporting this theory is the lack of sharp increases in H_2O molar densities that would indicate rapid increases in pressure and/or significant production of H_2O .

The higher overall measured temperatures and molar densities for the 0.32-kg s^{-1} MFR as well as the more significant sudden increases in temperature suggest that the detonation-wave axial height has increased to the point, where its effects begin to be observable at the upstream measurement location at intermediate MFR conditions. However, since the average measured temperature and molar densities as well as the magnitude of the temperature swings are much less than those of the high-MFR conditions, it is probable that the laser beam is capturing only the edge effects of the detonation-wave passage at this MFR. This is supported by the short duty cycle of the spikes of the H_2O number densities.

The maximum measured temperature and molar densities do not differ significantly for the 0.61- and 0.86-kg s^{-1} MFR conditions, indicating that the height of the detonation wave extends well beyond the measurement location for both conditions. However, the shape of the temperature versus time plots is quite different for these two cases. The typical decrease in measured temperature after the passage of the detonation wave is a result of the replacement of the detonated gases with new low-temperature reactants. The highest MFR condition is a two-wave operating condition. Because the cycle frequency of this condition is significantly higher, fresh cold charge cannot completely replace the detonated products before the passage of the next detonation wave. The result is smaller swings in gas temperatures between detonations.

Figure 7 displays temperature versus time for the 0.32- and 0.61-kg s^{-1} MFR conditions for both the upstream (25.4 mm) and downstream (50.8 mm) measurement locations. Since the upstream and downstream measurements were obtained separately in multiple tests rather than simultaneously, minor discrepancies in phasing and cycle frequency are apparent between each test pair. Figure 7 also provides evidence that the detonation-wave height is a strong driver of gas temperature at a given measurement location. For example, the lowest MFR (0.32 kg s^{-1}) shows the largest drop in temperature as the gas moves from the upstream to the downstream measurement location ($\sim 220 \text{ K}$ drop in average temperature). As the MFR increases to 0.61 kg s^{-1} , this axial temperature gradient is significantly reduced ($\sim 70 \text{ K}$ drop in average temperature), suggesting that the detonation front extends well past the upstream measurement location to near the downstream measurement location.

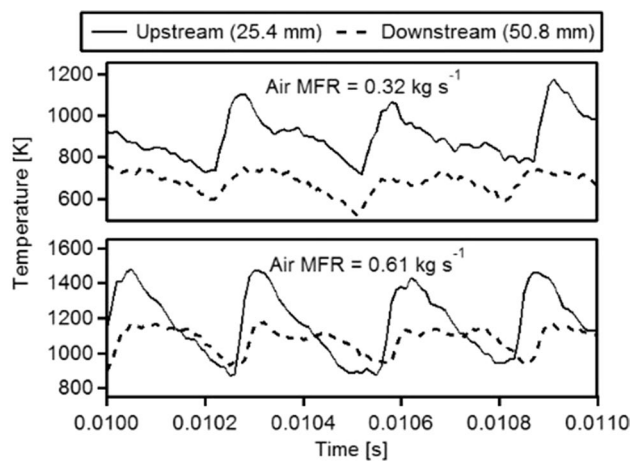


Fig. 7 Temperature versus time for two air MFRs at both the upstream (25.4 mm aft of the fuel plenum) and the downstream (50.8 mm aft of the fuel plenum) measurement locations

4 Conclusion

An all-fiber-based sensor that employs a single MEMS-tunable VCSEL source has been used to measure temperature and H_2O number densities in the detonation channel of an RDE at 100 kHz. A key component in the success of this measurement was the optical-access strategy that employed a custom-built, SMF/MMF dual-core fiber. The SMF core fiber in this arrangement was used to pitch laser light into the RDE channel. This light was retroreflected off the mirror-polished inner body of the RDE, and subsequently collected by the second core of the same fiber.

The temperature and concentration measurements were accomplished by fitting obtained H_2O absorption spectra to simulations based on the HITEMP molecular-line list. In this work, the MEMS-VCSEL system provided cycle-resolved simultaneous measurements of gas temperature and H_2O molar densities in an RDE at many different operating conditions. A wide range of temperatures was observed, depending on the reactant mass-flow rates and the axial location of the measurement beam. The overall trends agree with previously published modeling data [29]. At the upstream location, a large spike and subsequent decline in temperature is observed. Downstream, the fluctuation in temperature is much less extreme.

The measurement strategy outlined within this document could be improved in several ways. First, simultaneous measurements at multiple axial location would improve understanding of the behavior of the detonation process occurring within the annulus. In addition, a faster MEMS-VCSEL sweep rate would also be advantageous to better capture the effects occurring in the leading edge of the detonation wave. Likewise, faster data acquisition would improve the spectral resolution of the measurement

and may allow for the determination of gas pressures using the measured linewidths of the individual spectral features. Finally, measurements of other absorbing combustion species, such as CO or CO_2 , would provide additional insight into the efficacy of the combustion process in the RDE.

Acknowledgements Funding for this research was provided by the Air Force Research Laboratory (AFRL) under contract Nos. FA8650-10-C-2112 and FA8650-15-D-2580. The authors would like to thank Andrus Ionio of the Air Force Institute of Technology and Brian Sell and John Hoke of Innovative Scientific Solutions Inc. for setting up and operating the rotating detonation engine. Approved for public release: distribution unlimited (88ABW-2015-5934).

References

1. K. Kailasanath, *AIAA J* **38**, 1698 (2000)
2. D.A. Schwer, K. Kailasanath, *AIAA Pap* **581**, 2011 (2011)
3. F. K. Lu, E. M. Braun, L. Massa, and D. R. Wilson, in *47th AIAA/ASME/SAE/ASEE Jt. Propuls. Conf. Exhib.* (2011).
4. S. Sanders, D. Mattison, L. Ma, J. Jeffries, R. Hanson, *Opt. Express* **10**, 505 (2002)
5. S.T. Sanders, J.A. Baldwin, T.P. Jenkins, D.S. Baer, R.K. Hanson, *Proc. Combust. Inst.* **28**, 587 (2000)
6. D.W. Mattison, C.M. Brophy, S.T. Sanders, L. Ma, K.M. Hinckley, J.B. Jeffries, R.K. Hanson, *J. Propuls. Power* **19**, 568 (2003).
7. A.W. Caswell, S. Roy, X. An, S.T. Sanders, F.R. Schauer, *J.R. Gord, Appl. Opt.* **52**, 2893 (2013).
8. C. McGahan, B. Tom, A. Caswell, J. Gord, F. Schauer, and J. Hoke, in *52nd AIAA Aerosp. Sci. Meet. Natl. Harb. MD, AIAA-2014-0391* (2014).
9. C.S. Goldenstein, C.A. Almodóvar, J.B. Jeffries, R.K. Hanson, C.M. Brophy, *Meas. Sci. Technol.* **25**, 105104 (2014)
10. M.S. Wu, E.C. Vail, G.S. Li, W. Yuen, C.J. Chang-Hasnain, *Electron. Lett.* **31**, 1671 (1995).
11. M.S. Wu, E.C. Vail, G.S. Li, W. Yuen, C.J. Chang-Hasnain, *Photonics Technol. Lett. IEEE* **8**, 98 (1996).
12. B.A. Stein, V. Jayaraman, J.Y. Jiang, A. Cable, S.T. Sanders, *Appl. Phys. B* **108**, 721 (2012).
13. V. Jayaraman, B. Potsaid, J. Jiang, G.D. Cole, M.E. Robertson, C.B. Burgner, D.D. John, I. Grulkowski, W. Choi, T.H. Tsai, and others, in *SPIE Microtechnologies* (2013), p. 87630H–87630 H.
14. T. Kraetschmer, D. Dagel, S.T. Sanders, *Opt. Lett.* **33**, 738 (2008)
15. D.S. Baer, M.E. Newfield, N. Gopaul, R.K. Hanson, *Opt. Lett.* **19**, 1900 (1994)
16. L.A. Kranendonk, X. An, A.W. Caswell, R.E. Herold, S.T. Sanders, R. Huber, J.G. Fujimoto, Y. Okura, Y. Urata, *Opt. Express* **15**, 15115 (2007)
17. J. C. Shank, P.I. King, J. Karnesky, F. Schauer, J.L. Hoke, in *50th AIAA Aerosp. Sci. Meet. Incl. New Horizons Forum Aerosp. Expo. AIAA Pap.* (2012).
18. A. Naples, J. Hoke, J. Karnesky, and F. Schauer, in *51st AIAA Aerosp. Sci. Meet. Incl. New Horizons Forum Aerosp. Expo. AIAA Pap.* (2013).
19. J.M. Whitney, K. Takami, S.T. Sanders, Y. Okura, *Sens. J. IEEE* **11**, 3295 (2011)
20. L.A. Kranendonk, A.W. Caswell, S.T. Sanders, *Appl. Opt.* **46**, 4117 (2007).
21. L.S. Rothman, I.E. Gordon, Y. Babikov, A. Barbe, D. Chris Benner, P.F. Bernath, M. Birk, L. Bizzocchi, V. Boudon, L.R. Brown, *J. Quant. Spectrosc. Radiat. Transf.* **130**, 4 (2013).

22. G. Schulze, A. Jirasek, M.M.L. Yu, A. Lim, R.F.B. Turner, M.W. Blades, *Appl. Spectrosc.* **59**, 545 (2005).
23. J.J. Olivero, R.L. Longbothum, J. Quant. Spectrosc. Radiat. Transf. **17**, 233 (1977).
24. L.S. Rothman, I.E. Gordon, R.J. Barber, H. Dothe, R.R. Gamache, A. Goldman, V.I. Perevalov, S. A. Tashkun, J. Tennyson, *J. Quant. Spectrosc. Radiat. Transf.* **111**, 2139 (2010).
25. M.S. Wooldridge, P.V. Terek, M.T. Donovan, D.L. Hall, T.A. Miller, T.R. Palmer, C.R. Schrock, *Combust. Flame* **131**, 98 (2002).
26. B. J. McBride, S. Gordon, *NASA Ref. Publ.* **1311**, 84 (1996).
27. B.A. Rankin, D.R. Richardson, A.W. Caswell, A. Naples, J.L. Hoke, F.R. Schauer, in *53rd AIAA Aerosp. Sci. Meet. Kissimmee, FL* (2015).
28. B.A. Rankin, M.L. Fotia, D.E. Paxson, J.L. Hoke, F.R. Schauer, in *53rd AIAA Aerosp. Sci. Meet. Kissimmee, FL* (2015).
29. D.E. Paxson, in *52nd AIAA Aerosp. Sci. Meet. AIAA Pap.* (2014).